AIAA 81-1247R

Flow Separation in Shear-Layer-Driven Cavities

Julius Brandeis*
NASA Ames Research Center, Moffett Field, Calif.

A study of the shear-layer flow over a range of open-top cavity configurations is reported. Emphasis is placed on the effect that altering the cavity's span length and aspect ratio has on the development of the shear layer. Computational results are obtained using an interactive method which adapts the compressible boundary-layer model for the flow above the cavity and incompressible Navier-Stokes equations within the enclosure. Interaction of this composite model with the outer, inviscid supersonic flow is also considered in one case. The results show that the location of the stagnation points is sensitive primarily to the variation of the span. When the span was fixed and the aspect ratio varied, the shear layer was nearly unaffected except at aspect ratios less than 0.5. Interaction with the outer flow had a smoothing effect on the shape of the dividing streamline, but did not significantly affect the location of the stagnation points.

Nomenclature

a = speed of sound $= \sqrt{\gamma RT}$
AR = aspect ratio, $= H/L$
c_p = specific heat at constant pressure
H = height of the cavity
h = distance along the cavity's vertical wall measured from the convex corner
k = thermal conductivity
L = characteristic length
M = Mach number, $= u/a$
Pr = Prandtl number, $= \mu c_p/k$
p = pressure
R = constant in perfect gas law
Re = Reynolds number, $= \rho UL/\mu$
T = temperature
t = time
U = freestream velocity vector
u = velocity component in the x direction
v = velocity component in the y direction
x = Cartesian coordinate parallel to the plate
y = Cartesian coordinate normal to the plate
γ = ratio of specific heats, $= c_p/c_v$
Δ = small increment, difference
δ = boundary-layer thickness
ζ = vorticity function
μ = viscosity coefficient in the boundary-layer equations
ρ = density
ψ = stream function

Subscripts

BL = boundary-layer calculation
c = cavity calculation
e = local outer flow condition
R = reference
W = wall

Introduction

In this paper several aspects of the shear layer produced by a compressible external stream flowing over rectangular cavities (Fig. 1) are scrutinized. Close attention is paid to the variations of the location and shape of the dividing streamline as functions of the cavity's depth and span, and of the ratio of the two quantities (aspect ratio of the cavity). The influence of these parameters on the location of the stagnation points (separation and reattachment) is examined in detail.

Presented as Paper 81-1247 at the AIAA 5th Fluid and Plasma Dynamics Conference, Palo Alto, Calif., June 22-23, 1981; submitted July 14, 1981; revision received Nov. 12, 1981.

*NRC Research Associate. Present address: Lawrence Livermore National Laboratory, Livermore, California. Member AIAA.

The problem of the cavity flow driven by the external stream is one example of separated flow. In addition to being an instructive tool for furthering the understanding of the phenomenon of flow separation, this particular geometry occurs commonly as unwanted, drag-increasing gaps between segments of aircraft skin, as well as in slots between movable parts of wings and control surfaces. The gaps between the numerous tiles lining the outer surface of the space shuttle caused by the filler material evaporating at re-entry is yet another relevant example. On the other hand, the same flowfield may be utilized effectively and beneficially in laser-drilling operations for surface cooling and mass removal.

Although the cavity geometry is a standard test case used for validation of methods, few works were found in the literature addressing the problem of a shear-layer-driven cavity. Briefly, Mehta and Lavan[1] and O'Brien[2] obtained incompressible Navier-Stokes solutions to the flowfield in a channel containing a cavity in the lower wall. Weiss and Florsheim[3] developed a simplified model for the shear-layer-driven cavity flow based on assuming a straight dividing streamline having its stagnation points at the two convex corners. As will be shown, the method presently used is free from such restrictions. On the other hand, the specifics of the vortex structure have been studied in considerable detail, usually for the wall-driven cavities,[4-8] and no attempt will be made here to address that subject.

The flows considered in this work are two-dimensional and laminar with supersonic freestream. The flowfield is assumed to be steady. Although flows over cavities often exhibit unsteady behavior, the above assumption is felt to be well justified since small, fully viscous cavities of $L \sim \delta$ are considered. It is known[9] that cavities in which $L < 2\pi\delta$ do not resonate, and by keeping well below that limit, unsteadiness is not expected to be a problem. Furthermore, separated flows at supersonic speeds are known to be more stable than at subsonic speeds.

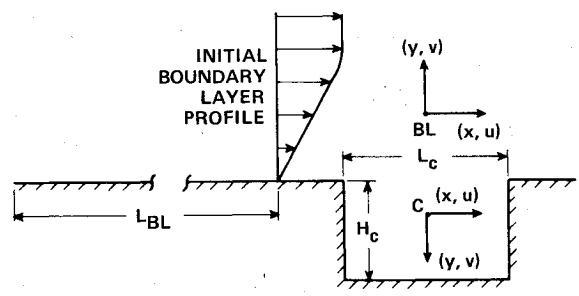

Fig. 1 Geometry and coordinate system for the interactive shear-layer-cavity computation.

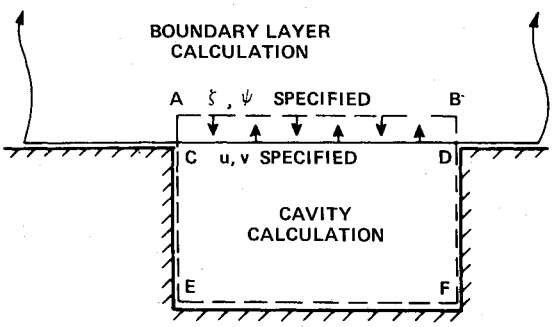

Fig. 2 Schematic of the overlapping regions used for matching.

Description of the Method

To study the problem described in the preceding section, the recently developed interactive zonal model is used.[10] This method is based on dividing the flowfield into two regions and then using an appropriate mathematical model in each region (Fig. 2). Thus, the parabolic boundary-layer equations of compressible, laminar flow are to be solved in the boundary-layer/shear-layer region. This region is assumed to be thin in order for the boundary-layer approximation to be valid. The governing equations (in two dimensions), nondimensionalized by the freestream reference quantities, are as follows.

Momentum:

$$\rho u \frac{\partial u}{\partial x} + \rho v \frac{\partial u}{\partial y} = -\frac{dp}{dx} + \frac{1}{Re}\frac{\partial}{\partial y}\left(\mu \frac{\partial u}{\partial y}\right) \tag{1}$$

Energy:

$$\rho u \frac{\partial T}{\partial x} + \rho v \frac{\partial T}{\partial y} = u \frac{dp}{dx} + \frac{1}{RePr}\frac{\partial}{\partial y}\left(\mu \frac{\partial T}{\partial y}\right) + \frac{\mu}{Re}\left(\frac{\partial u}{\partial y}\right)^2 \tag{2}$$

Continuity:

$$\frac{\partial(\rho u)}{\partial x} + \frac{\partial(\rho v)}{\partial y} = 0 \tag{3}$$

In addition, the equation of state and the viscosity relation are defined, respectively, as

$$p = \frac{\gamma - 1}{\gamma}\rho T \tag{4}$$

$$\mu = [(\gamma - 1)M_0^2]^{0.76} T^{0.76} \tag{5}$$

Equation (5) arises from the power law relation for viscosity in which the temperature ratio is raised to the power 0.76 after Chapman.[11]

The boundary conditions along the outer edge of the viscous layer are found from the appropriate compatibility relations, and the conditions on u and v along the interface are obtained through matching.

Within the region of reversed flow, the elliptic, incompressible Navier-Stokes equations are used. These constitute a valid model for the slowly recirculating flow encountered there, capable of dealing with stagnation points encountered at separation and reattachment of the dividing streamline. The Navier-Stokes equations, written in the vorticity-stream function form, are

$$\frac{\partial \zeta}{\partial t} = -u\frac{\partial \zeta}{\partial x} - v\frac{\partial \zeta}{\partial y} + \frac{1}{Re}\nabla^2 \zeta \tag{6}$$

$$\frac{\partial \psi}{\partial t'} = \nabla^2 \psi - \zeta \tag{7}$$

In Eq. (7), t' can be regarded as a nonphysical iteration time. Only the converged result (steady-state) is of interest. The boundary conditions at the three walls are the standard no-slip, impermeable wall conditions. Along the fluid interface the values of ψ and ζ are determined by matching. The numerical solution of Eqs. (1-5) is obtained by using the method of Reyhner and Flugge-Lotz.[12] Equations (6) and (7) were discretized using the fully explicit, second-order accurate forward time-center space (FTCS) numerical scheme.

The continuity of solution between the two regions must be insured by matching the flow variables at the interface. For this purpose, a matching model,[10] making use of partial overlap between the two computational regions, is utilized. The overlap, presented schematically in Fig. 2, facilitates matching not only the two velocity components, but $\partial u/\partial y$ as well. Furthermore, the present model allows the use of the second-order-accurate central-difference scheme for updating the boundary conditions, for these are always computed at internal points of the adjoining region. Consequently, no assumptions need to be made concerning the dividing streamline, which, together with its stagnation points, emerges naturally from the solution.

The interactive approach offers several advantages over the methods employing the general Navier-Stokes equations for solution of the total flowfield. For instance, using the parabolic boundary-layer equations, the limitations on the field size and cell Reynolds number are avoided in the shear layer, and no need exists for assuming the outflow boundary conditions. Furthermore, the interactive methods in general require significantly less computer processing time as well as less core space, making their use economically preferable.

To study the effects of pressure interaction, the model just described was coupled to an outer region in which the following exact irrotational flow equations were used:

$$(u^2 - a^2)\frac{\partial u}{\partial x} + uv\left(\frac{\partial u}{\partial y} + \frac{\partial v}{\partial x}\right) + (v^2 - a^2)\frac{\partial v}{\partial y} = 0 \tag{8}$$

$$\frac{\partial u}{\partial y} - \frac{\partial v}{\partial x} = 0 \tag{9}$$

where a denotes the speed of sound.

Solutions of this flowfield are conveniently obtained using the method of two-family characteristics.

The outer flow is then solved iteratively with the lower two layers until the convergence criterion on the slope of the matching boundary is met. Details pertaining to this procedure may be found in Ref. 13.

Procedure

To facilitate comparison between the various cases computed, all the results presented in this paper are for one set of outer flow conditions; namely, $Re_{BL} = 10^5$, $Pr = 1$, $M_\infty = 2.25$. The physical parameters varied were the cavity's length and depth. For computational purposes, the span of the cavity was adjusted by changing the number of grid points in the streamwise direction as well as by varying the step size, Δx. For all cases, the step size (Δy) in the direction normal to the freestream was held constant; therefore the depth of the cavity was controlled by changing the number of points. Both Δx and Δy were physically identical for the boundary-layer and cavity flows. The typical grid configuration for the cavity flowfield thus varied between 11×12 and 21×75 points. Within the boundary layer, 100 points were used in the direction normal to the flow. In the streamwise direction, the boundary-layer solution was initiated three steps upstream of the cavity and continued for three steps downstream from the cavity's trailing corner.

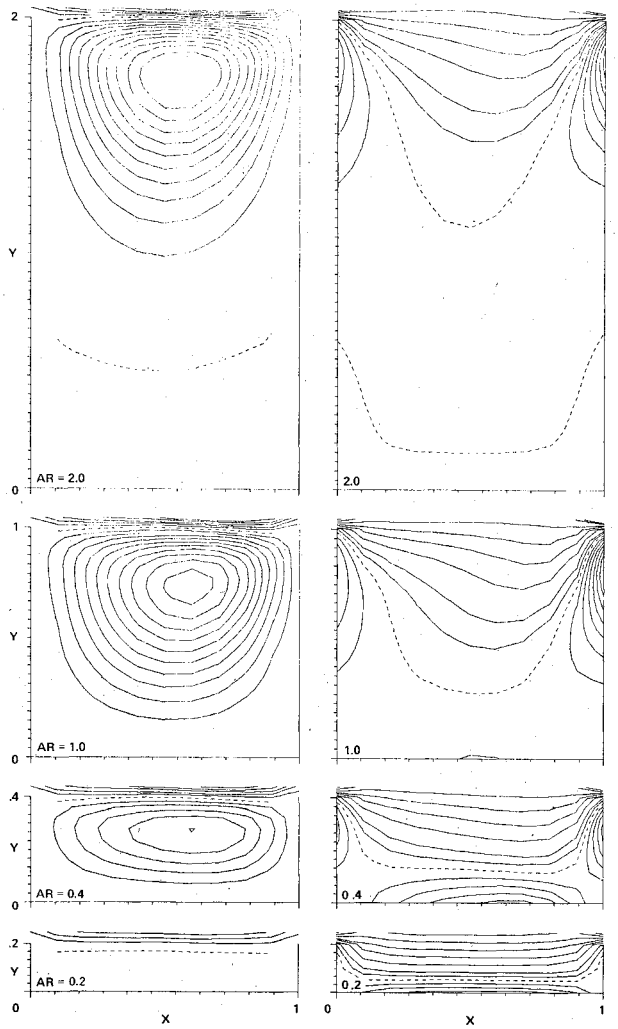

Fig. 3 Stream function (left) and vorticity (right) contour maps for several cavities of different aspect ratio but fixed span length.

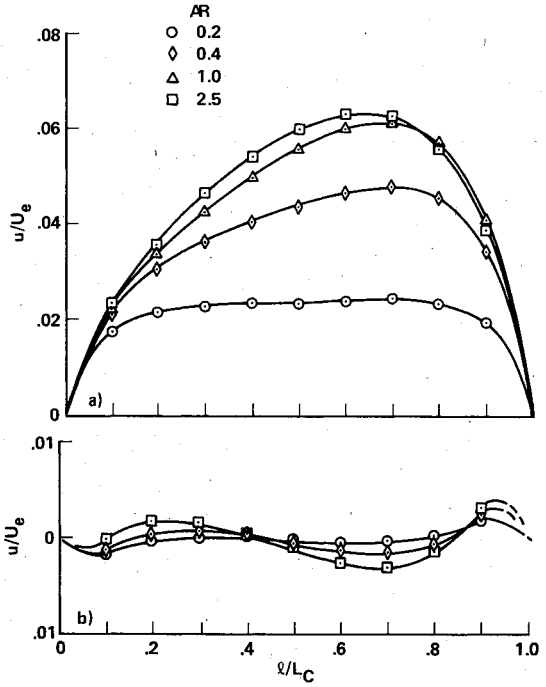

Fig. 4 Cavities of different aspect ratio but fixed span length: a) streamwise velocity component distribution along the open boundary; b) transverse velocity component distribution along the open boundary.

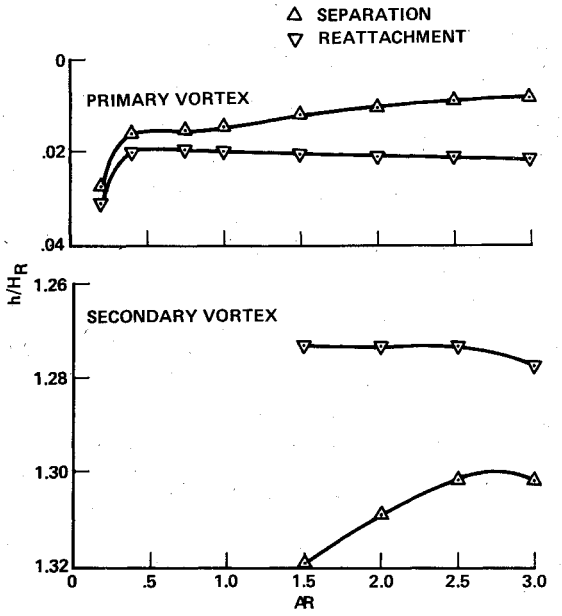

Fig. 5 Variation of stagnation point locations with the aspect ratio for cavities of fixed span length.

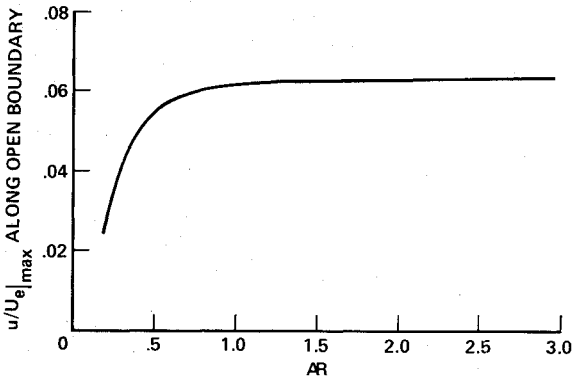

Fig. 6 Variation of maximum streamwise velocity found along the open boundary with aspect ratio for cavities of fixed span length.

The stagnation points of the dividing streamline were identified from the vorticity map as the points of intersection of the zero vorticity contour and the walls. In practice, the location of stagnation points was determined by linearly interpolating between two neighboring wall mesh nodes at which vorticity is of opposite algebraic sign.

Reference length L_R and reference height H_R were introduced for plotting the location of stagnation points to facilitate comparison between different cases with several varying parameters. The span and depth (L_R and H_R, respectively) for the reference configuration were arbitrarily taken as $H_R = L_R = 0.01 L_{BL}$.

Computations were carried out for cavities of aspect ratio ($AR = H/L$) ranging between 0.2 and 3.0 under the assumption that $dp/dx = 0$ in the outer flow (i.e., no pressure interaction). The results were divided into two groups for the purpose of clarity of presentation—all the cases included in the first category were computed for one cavity span, $L_c = L_R$, with H_c varied to affect the changes in aspect ratio. The second group consists of the cases for which H_c was held constant ($H_c = 0.4 H_R$) and L_c was altered to change the aspect ratio.

Pressure interaction was included in the computation of one cavity configuration ($L_c = 1.3 L_R$, $AR = 0.5$) in which the curvature of the interface streamlines indicated that the $dp/dx = 0$ assumption may be less valid for this case than it was in the other cases studied.

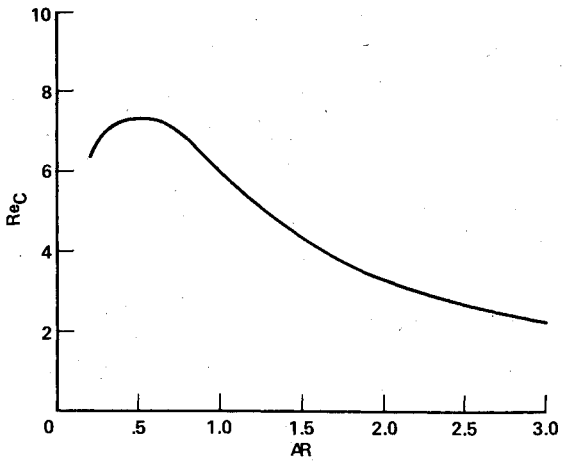

Fig. 7 Variation of the effective Reynolds number with aspect ratio for cavities of fixed span length.

Cavities of Constant Span Length

Figures 3-7 contain the results computed for a set of various aspect ratio cavities, all with equal span. The overall flowfield is best illustrated by the stream function and vorticity contour maps in Fig. 3. The streamwise and transverse velocity component distributions along the shear layer are shown in Fig. 4. These distributions were obtained along the line joining the convex corners of the cavity ($\overline{CD}$ in Fig. 2). Figure 5 presents the location of stagnation points along the cavity's vertical walls (relative to the convex corners) plotted as a function of the aspect ratio. Similarly plotted against the aspect ratio are the maximum values of the u-velocity component at the interface (Fig. 6) and the effective cavity Reynolds number (Fig. 7).

The general flow pattern exhibited in Fig. 3 is compatible with the results of Mehta and Lavan[1] who considered the flow in a two-dimensional channel containing a rectangular cavity. This is not unexpected. As has been shown in Ref. 10, the flow in the part of a cavity away from the shear layer is not very sensitive to the details of the structure of the shear layer itself, provided that certain criteria on mass inflow are observed.[9]

For shallow cavities (AR less than 0.5) it is apparent from Fig. 3 that an increase in aspect ratio results in an increase in the vortex strength, which may be expected to enhance mixing. This is easily explained from the physical viewpoint, as the wall boundary layers account for a decreasing fraction of the recirculating flow when the aspect ratio is increased. Consequently, the dividing streamline and its stagnation points are displaced upward, toward the open boundary of the cavity. Figure 5 shows, however, that for aspect ratios greater than 0.5, there is very little variation in the location of stagnation points. The vortex appears to have achieved a limit to its growth. Further increase in aspect ratio results in formation of small eddies in the concave corners which merge to form a secondary vortex, first observed at $AR = 1.5$. A still further increase in aspect ratio causes more vortex cells to appear. A tertiary vortex was observed at $AR = 3.0$.

The primary cell was found in the present study to have an aspect ratio of about 1.3 (Ref. 1 reports a value of 1.4). The primary vortex cell was found to be largest at its formation, and some contraction was observed thereafter as the aspect ratio was increased. This is evidenced by the upward displacement of the separation point of the secondary dividing streamline (the one separating the primary vortex from the secondary one) in Fig. 5. A very small change in the location of the primary separation point was observed in contrast to the much larger upward movement of the secondary separation point when the depth of the cavity was increased.

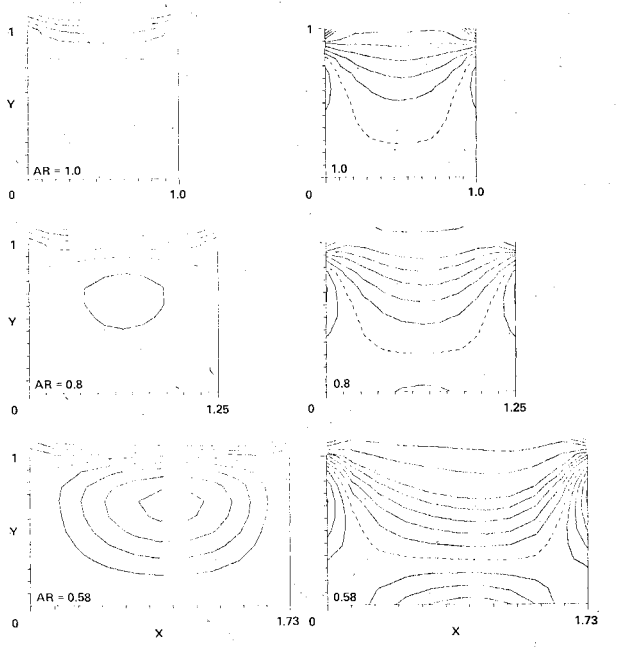

Fig. 8 Stream function (left) and vorticity (right) contour maps for several cavities of different aspect ratio but fixed depth.

At this point it is instructive to compare the computed location of the primary vortex center with the results of Ref. 3. For cavities with $AR = 1$ and 2, the present results are $y/H_c = 0.76$ and 0.90, respectively. This compares favorably with the values of 0.79 and 0.90 obtained in Ref. 3.

The plots of u- and v-velocity components at the open boundary (Fig. 4) show that the structure of the shear layer, though undergoing significant changes in response to change in cavity depth for $AR < 0.5$, is nearly invariant for $AR > 1.0$. The shear layer thus undergoes little change after the primary votex has achieved its optimum strength. For the shallow cavities, the mass flux through the open boundary (v distribution in Fig. 4b) is small and the corresponding u distribution (Fig. 4a) is flat as a consequence of the nearly flat dividing streamline. In contrast, for the deeper cavities the magnitudes of both u and v are larger and the u distribution loses its symmetry.

The Reynolds number was based on the average velocity within the cavity region. The drop in that quantity corresponding to the increase in aspect ratio exhibited in Fig. 7 is caused by the inclusion of an increasing quantity of low-energy fluid.

Cavities of Constant Depth

Graphical results analogous to those presented in the previous section are shown, this time for cavities having constant depth, in Figs. 8-10.

Again, the vortex strength dissipates because of viscous effects in the side boundary layers which, in the relative sense, grow as the enclosure diminishes in size (see Fig. 8). For the constant-depth cavities, the decrease in enclosed space is accomplished by decreasing the span and thus increasing the aspect ratio. The dividing streamline and its stagnation points now move deeper into the cavity, with an increase in aspect ratio (Figs. 10a and 10b) as the shear layer penetrates farther into the cavity. The interface u-velocity distribution (Fig. 9a) flattens out and decreases in magnitude as the aspect ratio increases (length decreases) for cavities with $AR \leq 1.0$. For the only shorter cavity presented in Fig. 9 ($AR = 1.3$), the magnitude of the interface velocity increases over that of the previous case and the middle section now becomes concave upward. The v-velocity distribution (Fig. 9b) shows a uniform increase in the magnitude of the crossflow as the span decreases. An explanation of the above results will be presented later.

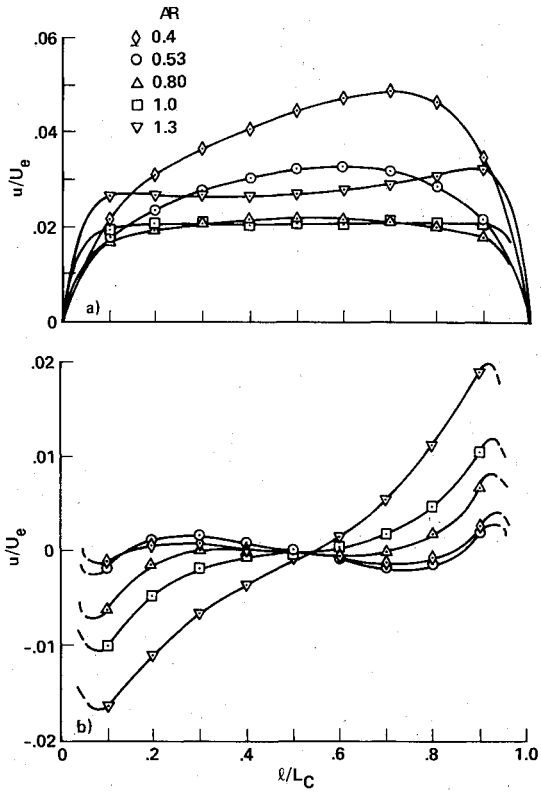

Fig. 9 Cavities of different aspect ratio but fixed depth: a) streamwise velocity component distribution along the open boundary; b) transverse velocity component distribution along the open boundary.

The general trends from Figs. 10a and 10b again show the separation and reattachment points occurring deeper in the cavity as the aspect ratio increases up to $AR = 1.0$. Beyond that limit, considerable discrepancy appears between the two sets of results computed with different step size Δx. At $AR = 1.6$, the results obtained with the finer grid spacing show the stagnation points moving slightly outward from the previous aspect ratio computed; with the coarser grid spacing, the stagnation points continue to move deeper into the cavity, almost linearly with the aspect ratio. The discrepancy between the two sets of results also exists in Figs. 10c and 10d where the effective Reynolds number and maximum interface u velocity are plotted against the aspect ratio. In these two graphs, however, the results differ only in magnitude and show consistent variation with aspect ratio. The maximum streamwise velocity component at the interface shows a parabolic-like variation with aspect ratio, with the minimum occurring at $AR \simeq 1.0$. The effective Reynolds number drops sharply in the lower aspect ratio range and levels off for $AR > 1.0$.

An explanation is now sought for the results in Figs. 10a-d with the aspect ratio exceeding unity. First, the possibility of numerical error is investigated. In general, the finer grid results are preferred, and they were chosen for the cases with $AR < 1$. Examination of vorticity values (ζ) at the corners, which were taken to coincide with the grid points, showed a significant dependence on Δx. As the streamwise step size was decreased, values of vorticity at the corner increased. The values of ζ upstream and downstream of each corner showed very little dependence on Δx, when they were taken at physically the same locations. Similar behavior was observed by Mehta and Lavan.[1] Thus, as Δx is decreased, the corner becomes better defined numerically. As the corner grows "sharper," the local acceleration of the flow increases abruptly (see Ref. 14 for further discussion). Since no special treatment is used at the corner grid points, the solution may be locally invalid there.

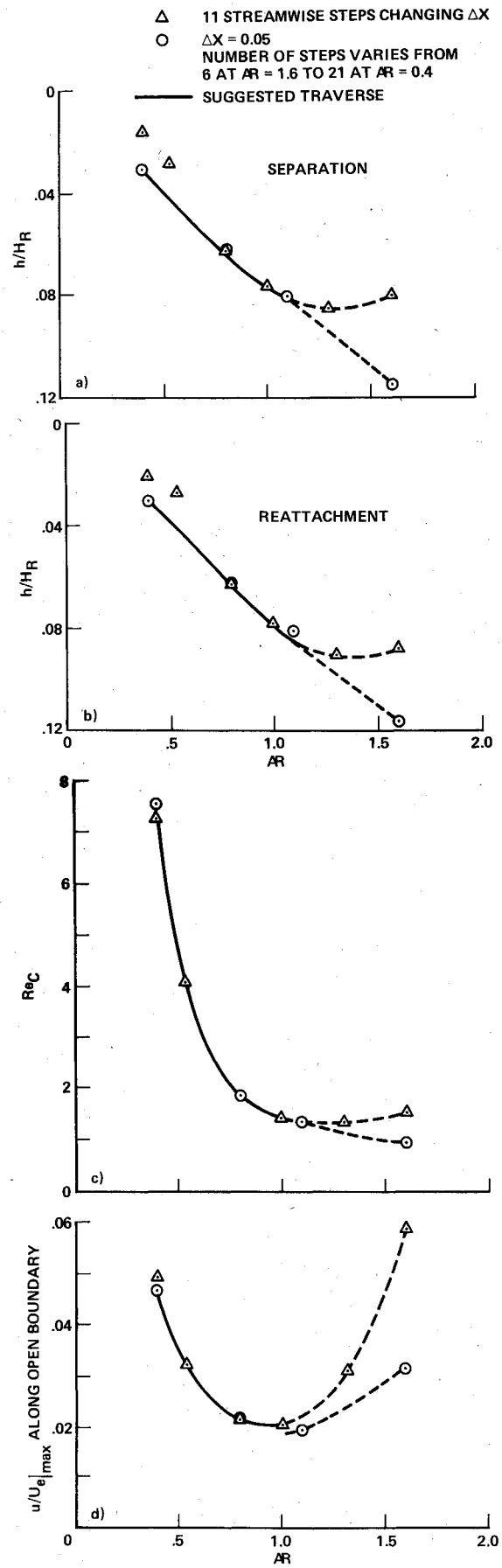

Fig. 10 Cavities of different aspect ratio but fixed depth: a) variation of separation point location with aspect ratio; b) variation of reattachment point location with aspect ratio; c) variation of the effective Reynolds number with aspect ratio; and d) variation of maximum streamwise velocity found along the open boundary with aspect ratio.

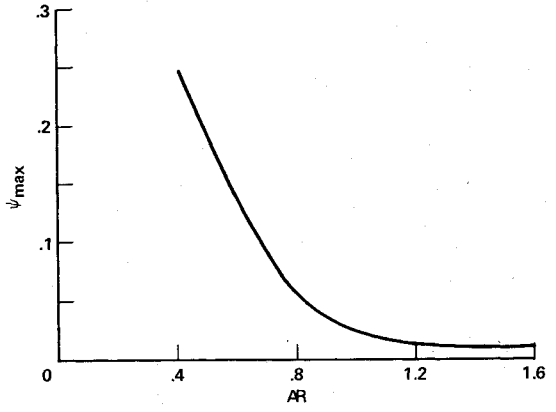

Fig. 11 Variation of vortex strength with aspect ratio for cavities of fixed depth.

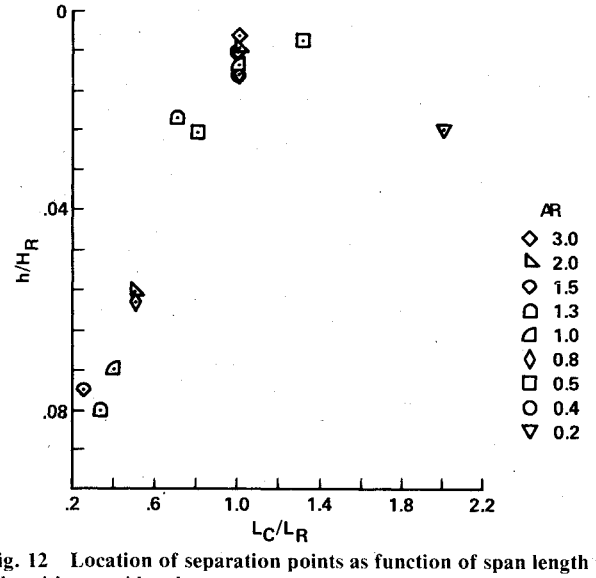

Fig. 12 Location of separation points as function of span length for all cavities considered.

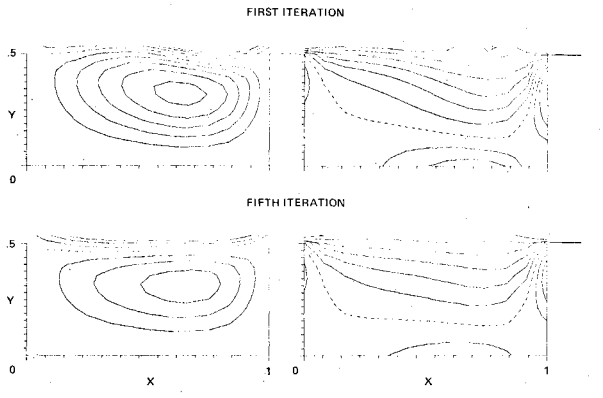

Fig. 13 Stream function (left) and vorticity (right) contour maps for the cavity having $AR=0.5$, $L_c/L_R=1.3$ with and without pressure interaction (fifth iteration indicates converged interactive result).

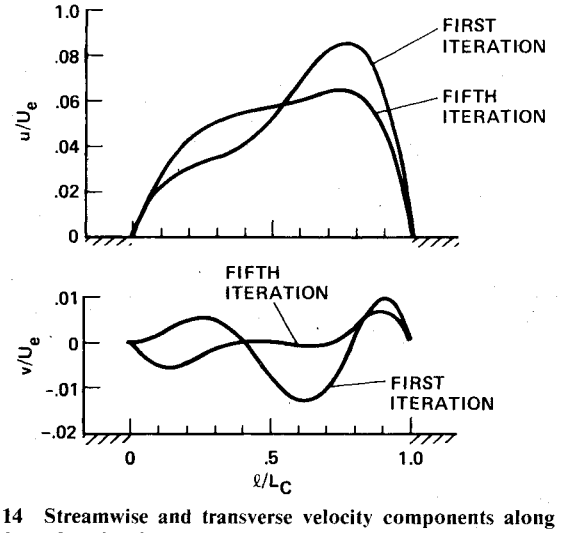

Fig. 14 Streamwise and transverse velocity components along the open boundary for the cavity in Fig. 13.

The location of the stagnation points is likewise affected by the variation of the corner vorticity with the step size. For the worst case ($AR=1.6$) this difference amounts to about 0.7 Δy (70% of one vertical mesh space). This, however, does not explain why the maximum interface u velocity shows growth regardless of step size Δx as the aspect ratio increases past $AR=1.0$ (Fig. 10d). A physical explanation may be given for this observation noting the inward movement of the stagnation points. As the shear layer penetrates deeper into the cavity with increasing aspect ratio, more of its higher-value streamlines are included below the open boundary. Taking into account the decreasing streamwise dimension of the cavity, this growth in interface velocities must reach a limit. In fact, the trapped vortex decreases in strength as the aspect ratio increases (as explained before), asymptotically approaching its minimum strength around $AR=1.2$. This is clearly seen in Fig. 11 in which the variation of the stream function value at the center of the vortex is plotted with the aspect ratio. An encouraging feature of this result is that it is (within plotting accuracy) independent of Δx.

Considering the above arguments and looking in retrospect at the results in Fig. 10, it is suggested that for $AR>1.0$ the coarser ($\Delta x=0.05=$ constant) grid data showing continuing inward movement of stagnation points and smaller increase in interface velocity may be more reliable. The implication, then, is that a small vortex cell may be forming below each corner. The numerical results, however, showed no evidence of such corner eddies.

Lastly, the location of the vortex center for $AR=1$ cavity is again compared with the corresponding result in Ref. 3. The present result is $y/H_c=0.66$, while Weiss and Florsheim[3] obtain $y/H_c=0.79$. This discrepancy once again indicated the significant effect due to the shear-layer penetration of the cavity, which is ignored in Ref. 3.

Dividing Streamline Separation and Reattachment

A common feature in all the cases presented was the containment of the dividing streamline and its stagnation points within the cavity region. The dividing streamline was always found to be convex upward, except in the vicinity of the stagnation points (the dividing streamline stagnated at right angle with the wall). These findings are consistent with the results of Roache and Mueller.[15]

It is common practice to link various aspects of the cavity flow behavior to the variation of Reynolds number. In the present study, where both H_c and L_c are varied, little consistent correlation was found between the cavity's Reynolds number and the locations of the stagnation points. Instead, it was possible to link the traverse of these points to the variation in the cavity's span.

Figure 12 shows the variation of separation point location with span for all cavity configurations considered hitherto. The location of these points is seen to be strongly dependent on the span of the cavity only. The aspect ratio (and thus the height) of the cavity affects the separation point only to a minor degree, when L_c does not change. This is most clearly seen in the case of $L_c/L_R=1.0$. In fact, the variation of separation point location with height changes (L_c constant)

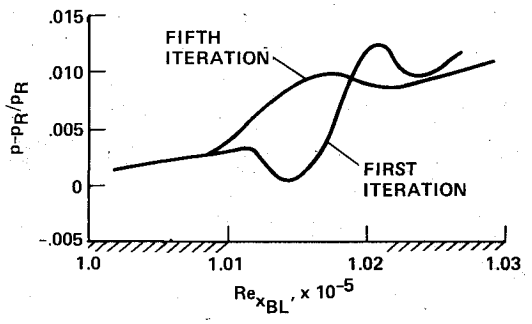

Fig. 15 Streamwise pressure distribution for the cavity in Fig. 13.

was no larger than the corresponding change caused by adjusting the step size Δx.

The aspect ratio does play the decisive role in the creation of the secondary vortices.

Influence of Pressure Interaction

In all the results presented thus far, it was assumed that there is no interaction with the outer flow, which is to say, $dp/dx=0$. It is of interest to see when and to what degree the pressure interaction affects the shear-layer cavity flow. The particular cavity geometry with $L_c/L_R=1.3$, $\mathcal{R}=0.5$ was chosen because the results with $dp/dx=0$ (first iteration of the present scheme) indicated a curvature of the dividing streamline likely to cause interaction with the outer field. After five cycles of the procedure referred to in an earlier section, the computation reached a state of acceptable convergence—changes due to further interaction were of the order of plotting accuracy. Figure 13 contains the comparison between the stream function and vorticity contour maps as they appeared in the first iteration and at convergence. It is apparent that pressure interaction had a considerable smoothing effect on the shear layer. The initially curved dividing streamline became almost a straight line. There was also a notable decrease in the strength of the vortex. Interaction similarly had a significant smoothing effect on the u and v velocity distributions along the open boundary (Fig. 14).

The pressure interaction lowered the separation point by about $0.5\Delta y$ ($0.02H_R$), and the location of the reattachment point was affected by less than $0.1\Delta y$.

The resulting spanwise pressure distribution is shown in Fig. 15. The magnitude of the pressure induced is rather small, but the shape of the converged pressure distribution is seen to be greatly different from that obtained after the first iteration.

The converged results in Fig. 13 appear to be quite similar to those presented in Figs. 3 and 8. In retrospect, it appears that neglecting the pressure interaction in the previous sections was justifiable.

Conclusion

Separation and reattachment were found to be located below the outer corners of the cavity. The dividing streamline was always found to be concave downward, except in the vicinity of the stagnation points where it was convex downward for separation and reattachment to take place at right angles with the wall. These observations agree with previous reports.

The locations of separation and reattachment points were found to be strongly dependent only on the span of the cavity. Varying the aspect ratio for a cavity of the given length had only a relatively minor influence on the locations of the stagnation points. For the fixed L case, the stagnation points were observed to move significantly only below $\mathcal{R}=0.5$. The movement of the stagnation points beyond $\mathcal{R}=0.5$ was small. This indicates that by the time the secondary vortex forms (between $\mathcal{R}=1$ and $\mathcal{R}=1.5$), the shear layer becomes insensitive to the changes in the cavity's height. This lack of sensitivity was ascertained to continue past the formation of the tertiary vortex (beyond $\mathcal{R}=2.5$).

The distribution of u velocity along the line joining the corners was found in general not to be symmetric. For the constant height cavity, the effect of decreasing the span length was to bring down the magnitude of u. A point was reached, however, where any further decrease in L caused an increase in u, because the effect of the dividing streamline being pushed into the cavity was greater than that due to decrease in length. When L was fixed and H varied, the u distribution grew flatter with a decrease in H (and thus in $\mathcal{R}$). Surprisingly, little change has occurred between $\mathcal{R}=1$ and $\mathcal{R}=2.5$, although H was increased 150%. It was in this region that a secondary vortex established itself.

The interaction of the flowfield with the inviscid outer flow had the effect of smoothing out any irregularities in the dividing streamline. In general, this interaction was found to be negligible for the cases considered.

References

[1] Mehta, U. B. and Lavan, Z., "Flow in a Two-Dimensional Channel with a Rectangular Cavity," NASA CR-1245, 1969.

[2] O'Brien, V., "Closed Streamlines Associated with Channel Flow over a Cavity," *The Physics of Fluids,* Vol. 15, Dec. 1972, pp. 2089-2097.

[3] Weiss, R. F. and Florsheim, B. H., "Flow in a Cavity at Low Reynolds Number," *The Physics of Fluids,* Vol. 8, Sept. 1965, pp. 1631-1635.

[4] Burggraf, O. R., "Analytical and Numerical Studies of the Structures of Steady Separated Flows," *Journal of Fluid Mechanics,* Vol. 24, Jan. 1966, pp. 113-151.

[5] Mills, R. D., "On the Closed Motion of a Fluid in a Square Cavity," *Journal of the Royal Aeronautical Society,* Vol. 69, Feb. 1965, pp. 116-120.

[6] Mills, R. D., "Numerical Solutions of the Viscous Flow Equations for a Class of Closed Flows," *Journal of the Royal Aeronautical Society,* Vol. 69, Oct. 1965, pp. 714-718.

[7] Kawaguti, M., "Numerical Solution of the Navier-Stokes Equations for the Flow in a Two-Dimensional Cavity," *Journal of the Physical Society of Japan,* Vol. 16, Nov. 1961, pp. 2307-2315.

[8] Pan, F. and Acrivos, A., "Steady Flows in Rectangular Cavities," *Journal of Fluid Mechanics,* Vol. 28, June 1967, pp. 643-655.

[9] Hankey, W. L. and Shang, J. S., "Analyses of Pressure Oscillations in an Open Cavity," *AIAA Journal,* Vol. 18, Aug. 1980, pp. 892-898.

[10] Brandeis, J. and Rom, J., "Interactive Method for Computation of Viscous Flow with Recirculation," *Journal of Computational Physics,* Vol. 40, No. 2, April 1981, pp. 396-410.

[11] Chapman, D. R., "Laminar Mixing of a Compressible Fluid," NASA Rept. 958, 1950.

[12] Reyhner, T. A. and Flugge-Lotz, I., "The Interaction of Shock Wave with a Laminar Boundary Layer," *International Journal of Non-Linear Mechanics,* Vol. 3, June 1968, pp. 173-199.

[13] Brandeis, J. and Rom, J., "Three Layer Interactive Method for Computing Supersonic Laminar Separated Flows," *AIAA Journal,* Vol. 18, Nov. 1980, pp. 1320-1327.

[14] O'Brien, V., "Parallel Shear Flows Over Cavities," Applied Physics Laboratory, The John Hopkins University TG 1138, Oct. 1970.

[15] Roache, P. J. and Mueller, T. J., "Numerical Solutions of Laminar Separated Flows," *AIAA Journal,* Vol. 8, Sept. 1970, pp. 530-538.